Ni and ZrO$_2$ promotion of In$_2$O$_3$ for CO$_2$ hydrogenation to methanol

Liang Liu, Yu Gao, Hao Zhang, Nikolay Kosinov, Emiel J.M. Hensen[*]

Laboratory of Inorganic Materials and Catalysis, Department of Chemical Engineering and Chemistry, Eindhoven University of Technology, P.O. Box 513, Eindhoven 5600 MB, the Netherlands

ABSTRACT

Transition metals, such as Ni, Pd, and Pt, and ZrO$_2$ are known as efficient promoters in M-In$_2$O$_3$-ZrO$_2$ catalysts for CO$_2$ hydrogenation to methanol. Herein, we systematically investigated the role of Ni and ZrO$_2$ promoters by preparing ternary NiO-In$_2$O$_3$-ZrO$_2$ catalysts and binary counterparts by flame spray pyrolysis. The highest methanol rate was obtained for the Ni(6 wt%)-In$_2$O$_3$(31 wt%)-ZrO$_2$(63 wt%) composition. DRIFTS-SSITKA shows that formate is the key intermediate in the hydrogenation of CO$_2$ to methanol. Kinetic analysis shows the competition between methanol and CO formation. The rate-limiting step in methanol formation is likely the hydrogenation of surface methoxy species. Ni and ZrO$_2$ play different promoting roles without showing synergy with respect to each other. Ni promotes hydrogenation of surface formate and methoxy species, while ZrO$_2$ maintains a high In$_2$O$_3$ dispersion, the smaller In$_2$O$_3$ size likely stabilizing formate and other intermediates during their conversion to methanol.

1. Introduction

Indium oxide (In$_2$O$_3$) is considered a promising catalyst for CO$_2$ hydrogenation to methanol, because it can be used in a wider temperature range than conventional Cu-Zn catalysts [1,2]. Mechanistically, methanol is thought to be formed by CO$_2$ adsorption and activation on oxygen vacancy sites (O$_v$) in In$_2$O$_3$, while adjacent In and O sites are involved in H$_2$ activation. Heterolytic H$_2$ dissociation on In$_2$O$_3$ leads to the formation of surface hydroxyl (O-H$^{\delta+}$) and indium hydride (In-H$^{\delta-}$). The hydride species can hydrogenate adsorbed CO$_2$ to formate, which is followed by stepwise hydrogenation to methanol in which protons are also involved [3,4]. In$_2$O$_3$ itself typically undergoes gradual deactivation during CO$_2$ hydrogenation [5]. While O$_v$ sites are formed by partial reduction of the In$_2$O$_3$ surface by hydrogen [6], over-reduction of In$_2$O$_3$ can lead to sintering of the In$_2$O$_3$ particles and even metallic In, which is especially prone to sintering [5]. Together these phenomena contribute to the catalyst deactivation.

Promoters can enhance the catalytic activity and structural stability of In$_2$O$_3$. Ni, Pd, and Pt provide active sites for H$_2$ dissociation, facilitating the hydrogenation of surface intermediates into methanol [7–9]. Such metals can also induce hydrogen spillover and assist in the surface reduction of In$_2$O$_3$, providing more O$_v$ sites for CO$_2$ adsorption. Zirconium oxide (ZrO$_2$) has been identified as promising structural promoter, serving as a support for In$_2$O$_3$. Frei et al. reported that In$_2$O$_3$ dispersed on monoclinic ZrO$_2$ (m-ZrO$_2$) shows a significantly higher methanol rate compared to In$_2$O$_3$ [10]. These authors argued that the lattice mismatch between the m-ZrO$_2$ support and the small In$_2$O$_3$ particles leads to enhanced formation of O$_v$. Yang et al. proposed that electron transfer from m-ZrO$_2$ to In$_2$O$_3$ can enhance H$_2$ dissociation on In$_2$O$_3$ and hydrogenation activity of surface intermediates toward methanol [11]. Besides, the structural stability of the In$_2$O$_3$ catalyst can be improved by supporting it on the m-ZrO$_2$ support. m-ZrO$_2$ has also been reported to stabilize and disperse the active InO$_x$ phase [12]. Furthermore, the authors stated that the high In$_2$O$_3$ dispersion on m-ZrO$_2$ and the specific interactions between In$_2$O$_3$ and ZrO$_2$ prevent over-reduction of In$_2$O$_3$ to metallic In at high reaction temperature.

Combining chemical and structural promoters can be a useful strategy to maximize the rate of methanol formation for CO$_2$ hydrogenation of In$_2$O$_3$ catalysts. Araújo et al. synthesized a Pd-In$_2$O$_3$-ZrO$_2$ catalyst by flame spray pyrolysis (FSP), which exhibited a nearly three times higher methanol formation rate than the binary Pd/In$_2$O$_3$ and In$_2$O$_3$/ZrO$_2$ reference catalysts [13]. The methanol formation rate linearly correlated with the concentration O$_v$ sites. Operando characterization showed that InPd$_x$ alloy particles, decorated by InO$_x$ layers, were formed during CO$_2$ hydrogenation [14]. Finally, it was postulated that CO$_2$ is activated on O$_v$ on InO$_x$, while H$_2$ is activated on InPd$_x$ sites [14]. Liu's group prepared a series of ternary M-In$_2$O$_3$-ZrO$_2$ catalysts (M = Ni, Rh, Pt and Au), which exhibited a higher methanol rate compared to their

binary M-In_2O_3 and In_2O_3-ZrO_2 counterparts [15–18]. Similar mechanistic explanations were put forward – the metal being responsible for H_2 activation and ZrO_2 inducing the formation of O_v sites on In_2O_3. This study also mentioned that the catalyst contains multiple structures of the promoting metal M, including single atoms, clusters and alloys with In. Due to this heterogeneity in the structure of the active M sites, it is challenging to derive accurate structure-performance relationship for methanol synthesis. Thus, there is a need for more defined ternary M-In_2O_3-ZrO_2 catalysts to systematically investigate the role of the different components in the catalytic mechanism of CO_2 hydrogenation to methanol.

In this study, we used a one-step flame spray pyrolysis (FSP) approach to obtain uniform NiO-In_2O_3-ZrO_2 mixed oxides. First, we optimized the ZrO_2 content for CO_2 hydrogenation to methanol. The optimal Ni-In_2O_3-ZrO_2 catalyst was significantly more active towards methanol formation than In_2O_3, In_2O_3-ZrO_2 and Ni-In_2O_3 reference catalysts. To resolve the promoting roles of Ni and ZrO_2 in the ternary NiO-In_2O_3-ZrO_2 system, a combination of spectroscopic tools and kinetic methods was employed. Operando diffuse reflectance infrared Fourier transform spectroscopy combined with steady-state isotopic transient kinetic analysis (DRIFTS-SSITKA) was used to follow the relevant surface intermediates for CO_2 hydrogenation to methanol.

2. Experimental section

2.1. Catalysts preparation

Ni-In_2O_3-ZrO_2 catalysts with a Ni content of 6.0 wt% and its counterparts (In_2O_3, ZrO_2, In_2O_3-ZrO_2 and Ni-In_2O_3) were prepared using a one-step flame spray pyrolysis (FSP) via a Tethis NPS10 setup. The precursor solution was prepared by dissolving appropriate amounts of In $(NO_3)_3 \cdot x H_2O$ (99.999 %, Alfa Aesar) and promoter complexes including $Ni(NO_3)_2 \cdot 6H_2O$ (98.5 %, Sigma Aldrich) and zirconium (IV) acetylacetonate (Sigma Aldrich) in a 1:1 (vol %) solvent mixture of ethanol (HPLC, Sigma Aldrich) and 2-ethylhexanoic acide (99 %, Sigma Aldrich) at room temperature. The total metal concentration in the precursor was maintained at 0.15 mol/L. The solution was pumped through a 0.4 mm nozzle at a flow rate of 1.0 mL/min, and dispersed into a flame with a flow of 1.5 L/min CH_4 and 3.0 L/min O_2. The prepared nanoparticles were collected on a glass-fiber filter (Hahnemühle FineArt GmbH, GF6, 257 mm in diameter). The samples are denoted by In_2O_3, ZrO_2, $In_2O_3(x)$-ZrO_2, Ni(6)-In_2O_3 and Ni(6)-$In_2O_3(x)$-ZrO_2, where x represents the In_2O_3 content (wt%).

2.2. Characterization

The textural properties of the as-prepared catalysts were analyzed by N_2 physisorption at −196 °C using a Micrometrics TriStar II 3020 instrument. The samples were pretreated at 120 °C in a N_2 flow overnight. The Brunauer-Emmett-Teller (BET) method was used to determine the specific surface area.

The chemical components of the catalyst were analyzed using Inductively coupled plasma optical emission spectroscopy (ICP-OES) (Ametek SPECTROBLUE EOP). Prior to measurements, the sample was dissolved in a 1:2.75 (by weight) mixture of $(NH_4)_2SO_4$/(concentrated) H_2SO_4 and diluted with water.

X-ray diffraction (XRD) measurements were performed using a Bruker D2 Phaser diffractometer with Cu Kα radiation (1.5406 Å) between 10 and 90° with a step size of 0.02° at 0.23 s/step scan rate.

Temperature-programmed reduction (H_2-TPR) measurements were carried out using a Micromeritics AutoChem II setup equipped with a thermal conductivity detector (TCD). An amount of 50 mg of sample was loaded into a quartz U-tube between two quartz wool layers and pretreated in a He flow (50 mL/min) at 120 °C for 1 h. TPR was performed in a flow of 4 vol % H_2 in He (50 mL/min), while increasing the temperature from 40 °C to 800 °C at a rate of 10 °C/min. The outlet gas was analyzed by a thermal conductivity detector (TCD). The H_2 consumption was calibrated based on CuO reference.

X-ray absorption spectroscopy (XAS) measurements at the Ni K-edge were carried out at the CLÆSS beamline of the ALBA synchrotron (Barcelona, Spain) with a Si(111) double-crystal monochromator. For sample preparation, the catalysts were appropriately diluted with boron nitride (BN), pressed into pellets and sealed in Kapton tape. The preparation of used samples for XAS characterization involved CO_2 hydrogenation in the reaction mixture ($CO_2/H_2/N_2$ = 10:30:10 mL/min) at 300 °C and 30 bar for 14 h, followed by release of the pressure to atmospheric pressure at 300 °C, cooling to room temperature in a N_2 flow of 50 mL/min and transfer to a glove-box without air exposure. The further sample preparation for XAS was done as above in the glove-box, followed by sealing of the holder by Kapton tape. The sample was analyzed at room temperature at a total pressure of ~0.07 mbar. For the XAS measurements, the sample was recorded in transmission mode. Ni foil and NiO references were measured simultaneously in transmission mode for energy calibration under the same conditions. The data analysis, including energy calibration, normalization, linear combination fitting (LCF) analysis and EXAFS fitting were carried out using the Demeter package (Athena/Artemis software). The relevant scattering paths were calculated with the FEFF6 code based on crystal structures of face-centered cubic (fcc) Ni metal, fcc NiO, and hexagonal Ni-In alloy. A Ni−In (oxidic) single scattering path was also incorporated in the EXAFS fitting [8]. The amplitude reduction factor (S_0^2) was obtained by fitting the Ni foil. The distance (ΔR), coordination number (CN), and Debye-Waller factor (σ^2) were fitted. The Fourier-transformed EXAFS are plotted without phase-correction.

In situ high-pressure IR spectroscopy measurements were performed in transmission mode using a Nicolet FT-IR spectrometer equipped with a cryogenic MCT detector. The sample pellets were obtained by diluting the catalyst with FSP-derived ZrO_2 (surface area of 204 m^2/g, tetragonal and monoclinic mixed phases) in a 1:10 ratio by mass. An amount of 15 mg of the diluted sample was pressed into a pellet and pretreated in a He flow of 100 mL/min at 260 °C for 1 h. After cooling to 40 °C in He, a background spectrum was collected. For in situ IR measurements at elevated pressure, the system was pressurized to 10 bar in CO_2/H_2 mixture (1:3, total flow 50 mL/min). Then, the system was heated to 300 °C and maintained for 1 h. Spectra were collected throughout the temperature-programmed and constant-temperature reaction steps. For subsequent temperature-programmed desorption measurements in He, the sample was cooled to 50 °C after temperature-programmed CO_2 hydrogenation. Then, the gas feed was switched from the reaction gas mixture (CO_2:H_2 = 1:3, 50 mL/min, 10 bar) to He (100 mL/min, 1 bar) at 50 °C, followed by heating to 400 °C in He, while collecting IR spectra.

Operando diffuse reflectance infrared Fourier transform spectroscopy (DRIFTS) experiments were performed in a Vertex 70 v FT infrared spectrometer (Bruker) equipped with an MCT detector, mid-IR laser source and a Praying Mantis™ accessory and cell (Harrick). An amount of 10 mg catalyst was placed on the top of the SiC layer in the cell. The sample was pretreated in an Ar flow of 50 mL/min at 260 °C, followed by recording a background spectrum. The catalyst was tested in reactant mixture (CO_2:H_2:Ar = 1:3:1, 50 mL/min, 1 bar) at 260 °C until a steady state is reached. The transient experiments were performed by switching the $^{12}CO_2/H_2$ feed to a $^{13}CO_2/H_2$ one at 260 °C. Ne was used as a tracer to account for the gas phase hold-up in the system. The gas composition after passing through the catalyst bed was analyzed using MS (Balzer Prisma), with the MS capillary inlet positioned in close proximity to the catalyst bed. This configuration allowed rapid gas replacement during switches, ensuring equal gas hold-up times as confirmed by MS and IR measurements. The mean surface-residence time τ^p was calculated by integrating the time response of the ^{12}C/^{13}C replacement in products (CO and methanol) and intermediates (HCOO* and CO*) as respectively measured by MS and IR, using Eq. (1):

$$\tau^p \ = \ \int_0^\infty (F^p(t) - \ F^{Ne}(t)) \ dt \tag{1}$$

where F^p is the normalized transient response of the product P and F^{Ne} is the normalized transient response of the tracer Ne.

2.3. Catalytic activity measurements

The catalytic performance was evaluated in a down-flow stainless-steel reactor with an inner diameter of 4 mm. The catalyst was sieved into particles with a size range of 125–250 μm, loaded into the reactor and diluted with 200 mg SiC. Prior to the reaction, the sample was pretreated in He (50 mL/min) at 260 °C using a rate 5 °C/min followed by a dwell of 1 h. After pretreatment, the sample was exposed to the reaction mixture (20 % CO_2/60 % H_2/ 20 % N_2) and the pressure in the reactor was increased to 30 bar using a back-pressure regulator. Apparent activation energies of methanol and CO formation were determined by adjusting the temperature in the range from 256 to 264 °C with steps of 2 °C at 30 bar (CO_2:H_2:N_2 = 1:3:1, 50 mL/min). To determine the reaction orders with respect to CO_2 or H_2 for methanol and CO formation, the CO_2 or H_2 flows were adjusted, while using a N_2 flow to balance the total flow rate (total flow 50 mL/min). To prevent condensation of products, the outlet gas line was kept at 130 °C. The product composition was analyzed by an online gas chromatograph (Interscience, CompactGC) equipped with Rtx-1 (FID), Rt-QBond and Molsieve 5 A (TCD), and Rt-QBond (TCD) columns. Response factors $f(i)$ for each compound i, respective to the internal standard of N_2, in the GC analysis were determined by Eq. (2):

$$f(i) \ = \ \frac{A(i) \ \times \ F(N_2)_{in}}{A(N_2) \ \times \ F(i)_{in}} \tag{2}$$

where $A(i)$ is the integrated area determined for the peak of compound i, and $F(i)_{in}$ is the corresponding known volumetric flow rate at the reactor inlet. The unknown effluent volumetric flow rate of product was determined using Eq. (3):

$$F(i)_{out} \ = \ \frac{A(i)}{A(N_2) \ \times \ f(i)} \ \times \ F(N_2)_{out} \tag{3}$$

The CO_2 conversion (X), product selectivity (S) and product formation rate (r) were calculated using the following equations:

$$X(CO_2) \ = \ \frac{F(CO)_{out} \ + \ F(CH_3OH)_{out} \ + \ F(CH_4)_{out}}{F(CO_2)_{out} \ + \ F(CO)_{out} \ + \ F(CH_3OH)_{out} \ + \ F(CH_4)_{out}} \tag{4}$$

$$S(product) \ = \ \frac{F(product)_{out}}{F(CO)_{out} \ + \ F(CH_3OH)_{out} \ + \ F(CH_4)_{out}} \tag{5}$$

$$STY(CH_3OH) \ = \ \frac{F(CH_3OH)_{out} \ \times \ Mw(CH_3OH)}{V_m \ \times \ m_{cat}} \tag{6}$$

where F stands for the volumetric flow rate determined based on the N_2 internal standard using calibrated response factors, $Mw_{(CH3OH)}$ is the molecular weight of methanol and V_m is the molar volume of ideal gas at standard conditions.

3. Results and discussion

3.1. Characterization as-prepared Ni-In₂O₃-ZrO₂

We prepared Ni-In_2O_3-ZrO_2 samples at different ZrO_2 contents (8–84 wt%) using FSP. A Ni content (metal basis) of 6.0 wt% was chosen, as this Ni content previously led to the highest methanol rate for the Ni-In_2O_3 system prepared by FSP [8]. The In_2O_3, Ni(6)-In_2O_3 and In_2O_3-ZrO_2 reference samples were prepared in the same manner. The actual content of metal and metal oxide was similar to the theoretical content, as evidenced by elemental analysis (Table S1). XRD patterns of

all these samples are collected in Fig. S1. The main crystalline phase in In_2O_3 and Ni(6)-In_2O_3 is cubic In_2O_3 without any diffraction lines of Ni-containing phases. At a ZrO_2 content below 44 wt%, In_2O_3 is also the dominant phase in the Ni-In_2O_3-ZrO_2 samples. At higher ZrO_2 content, the diffraction lines shift to lower angles in the In_2O_3(33)-ZrO_2 and Ni-In_2O_3-ZrO_2 samples. These changes indicate an increasing contribution of tetragonal ZrO_2 (t-ZrO_2) phase, which exhibits diffraction lines close to those of cubic In_2O_3, in line with an earlier study [10]. The only crystalline phase observed in Ni(6)/ZrO_2 is t-ZrO_2 phase. The absence of other diffraction lines points to the high dispersion of Ni on ZrO_2.

Average crystallite sizes estimated by the Scherrer equation and BET surface areas are given in Table 1. Compared to In_2O_3 with an average particle size of 5.6 nm, the as-prepared In_2O_3(33)-ZrO_2, Ni(6)-In_2O_3-ZrO_2 and Ni(6)-In_2O_3 samples contain slightly smaller In_2O_3/t-ZrO_2 particles with sizes between 4.0 and 5.3 nm. For the as-prepared In_2O_3, Ni(6)-In_2O_3, and Ni(6)-In_2O_3(31)-ZrO_2 samples, the In_2O_3 particle size determined by Rietveld refinement is comparable to the average crystallite size estimated by the Scherrer equation (Table 1 and S2). Despite there is no obvious trend between the crystallite size and the Zr content, the surface areas of the Ni-In_2O_3-ZrO_2 samples increases from 170 m²/g for Ni(6)-In_2O_3 to 227 m²/g for Ni(6)-In_2O_3(10)-ZrO_2 with increasing Zr content.

3.2. Catalytic performance of CO₂ hydrogenation

The influence of the ZrO_2 content on the catalytic performance of the Ni-In_2O_3-ZrO_2 samples was evaluated in CO_2 hydrogenation at temperature of 260 °C, pressure of 30 bar, H_2/CO_2 ratio of 3 and weight-hourly space velocity (WHSV) of 30,000 mL g_{cat}^{-1} h^{-1}. The results of these activity measurements are given in Table 2. The methanol rate exhibits a maximum of 0.33 g_{MeOH} g_{cat}^{-1} h^{-1} at a ZrO_2 content of 64 wt% in the Ni(6)-In_2O_3(31)-ZrO_2 catalyst. The methanol selectivity of this catalyst is 51.8 % with CO (47.8 %) and CH_4 (0.4 %) being the other reaction products. The Ni(6)-ZrO_2 presents a CH_4 selectivity of nearly 100 % with CO as a minor side-product (0.03 %). Moreover, the CO_2 conversion of Ni(6)-ZrO_2 is much higher (82 %) than that of Ni(6)-In_2O_3(31)-ZrO_2 (7.5 %). These substantial differences can be explained by the formation of metallic Ni nanoparticles in Ni(6)-ZrO_2 that are large enough to catalyze CO_2 methanation [8,19,20]. As the reduced Ni

Table 1

Physicochemical properties of the as-prepared and used In_2O_3-based samples.

Sample	d_{XRD} (nm)[a] As-prepared[b]	Specific surface area (m²·g⁻¹)	d_{XRD} (nm)[a] Used[c]	Specific surface area (m²·g⁻¹)
In_2O_3	5.6	150	12.5	67
In_2O_3(33)-ZrO_2	5.3	190	5.8	173
Ni(6)-In_2O_3	4.3	170	19.1	36
Ni(6)-In_2O_3(86)-ZrO_2	3.8	165	11.2	76
Ni(6)-In_2O_3(68)-ZrO_2	5.0	169	11.8	111
Ni(6)-In_2O_3(50)-ZrO_2	4.0	195	8.6	140
Ni(6)-In_2O_3(31)-ZrO_2	4.4	187	5.0	142
Ni(6)-In_2O_3(10)-ZrO_2	4.0	227	4.3	180
Ni(6)-ZrO_2	4.0	236	6.7	110

[a] Particle size based on XRD line broadening.
[b] As-prepared samples prepared by FSP.
[c] After CO_2 hydrogenation (300 °C, 30 bar, CO_2/H_2/N_2 = 10/30/10 mL/min, 12 h).

Table 2
Catalytic performance for Ni-In$_2$O$_3$-ZrO$_2$ samples.[a]

Sample	CO$_2$ conversion (%)	Selectivity			Methanol rate (g_{MeOH} g_{cat}^{-1} h^{-1})
		S (MeOH) (%)	S (CO) (%)	S (CH$_4$) (%)	
Ni(6)-In$_2$O$_3$	5.2	45.2	54.7	0.1	0.20
Ni(6)-In$_2$O$_3$(86)-ZrO$_2$	6.2	42.4	57.4	0.2	0.23
Ni(6)-In$_2$O$_3$(68)-ZrO$_2$	6.4	45.9	53.8	0.3	0.25
Ni(6)-In$_2$O$_3$(50)-ZrO$_2$	7.0	48.0	51.7	0.3	0.29
Ni(6)-In$_2$O$_3$(31)-ZrO$_2$	7.5	51.8	47.8	0.4	0.33
Ni(6)-In$_2$O$_3$(10)-ZrO$_2$	6.1	23.5	76.3	0.3	0.12
Ni(6)-ZrO$_2$	81.6	0.0	0.0	100.0	0.00

[a] Reaction conditions: 260 °C, 30 bar, CO$_2$/H$_2$/N$_2$ = 10/30/10 mL/min, and WHSV = 30,000 mL h^{-1} g$_{cat}^{-1}$, 12 h.

particles in Ni-In$_2$O$_3$ and Ni-In$_2$O$_3$-ZrO$_2$ catalysts are much smaller, CH$_4$ formation is suppressed. The active sites at the Ni-In$_2$O$_3$ interface catalyze methanol and CO formation.

We then compared the catalytic performance of Ni(6)-In$_2$O$_3$(31)-ZrO$_2$, In$_2$O$_3$, Ni(6)-In$_2$O$_3$, In$_2$O$_3$(33)-ZrO$_2$ in CO$_2$ hydrogenation (30 bar, H$_2$/CO$_2$ = 3, WHSV = 60,000 mL g$_{cat}^{-1}$ h^{-1}) at 260 and 300 °C (Fig. 1). The In$_2$O$_3$(33)-ZrO$_2$ and Ni(6)-In$_2$O$_3$(31)-ZrO$_2$ samples have the same In/Zr ratio of 3/7. The CO$_2$ conversion increases from 0.7 % for In$_2$O$_3$ to 1.5 % for In$_2$O$_3$(33)-ZrO$_2$, 3.2 % for Ni(6)-In$_2$O$_3$ and 5.2 % for Ni(6)-In$_2$O$_3$(31)-ZrO$_2$ at 260 °C. In$_2$O$_3$ and In$_2$O$_3$(33)-ZrO$_2$ exhibit a similar methanol selectivity of ~65 %. The methanol selectivity for the Ni-containing catalysts is much lower, i.e., 46 % for Ni(6)-In$_2$O$_3$ and 51 % for Ni(6)-In$_2$O$_3$(31)-ZrO$_2$. At 300 °C, the CO$_2$ conversion of all the catalysts increased, while the methanol selectivity decreased due to the formation of more CO. The trends in CO$_2$ conversion and methanol selectivity at this temperature are comparable to those observed at 260 °C.

The methanol rates are depicted in Fig. 1c. The methanol rate of ~0.45 g_{MeOH} g_{cat}^{-1} h^{-1} for Ni(6)-In$_2$O$_3$(31)-ZrO$_2$ is nearly equal to the sum of the methanol rates of ~0.25 g_{MeOH} g_{cat}^{-1} h^{-1} for Ni(6)-In$_2$O$_3$ and ~0.17 g_{MeOH} g_{cat}^{-1} h^{-1} for In$_2$O$_3$(33)-ZrO$_2$ at 260 °C. Based on this consideration, there is no synergy between promotion by Ni and ZrO$_2$ for In$_2$O$_3$-catalyzed CO$_2$ hydrogenation. At 300 °C, the highest methanol rate of 0.55 g_{MeOH} g_{cat}^{-1} h^{-1} was observed for Ni(6)-In$_2$O$_3$(31)-ZrO$_2$, substantially higher than the rates observed for the binary references Ni(6)-In$_2$O$_3$ (0.34 g_{MeOH} g_{cat}^{-1} h^{-1}) and In$_2$O$_3$(33)-ZrO$_2$ (0.38 g_{MeOH} g_{cat}^{-1} h^{-1}). Fig. 1d shows the methanol rates normalized to the surface area of the used catalysts. For this purpose, we used the BET surface areas of samples after 12 h CO$_2$ hydrogenation at 300 °C. In$_2$O$_3$ and In$_2$O$_3$(33)-ZrO$_2$ exhibit similar area-normalized methanol rates, indicating that the main role of ZrO$_2$ is to disperse In$_2$O$_3$ better. Ni(6)-In$_2$O$_3$(31)-ZrO$_2$ has a slightly higher methanol rate than In$_2$O$_3$. However, a significantly higher normalized methanol rate was observed in the Ni(6)-In$_2$O$_3$ catalyst compared to Ni(6)-In$_2$O$_3$(31)-ZrO$_2$. The lower efficiency of Ni
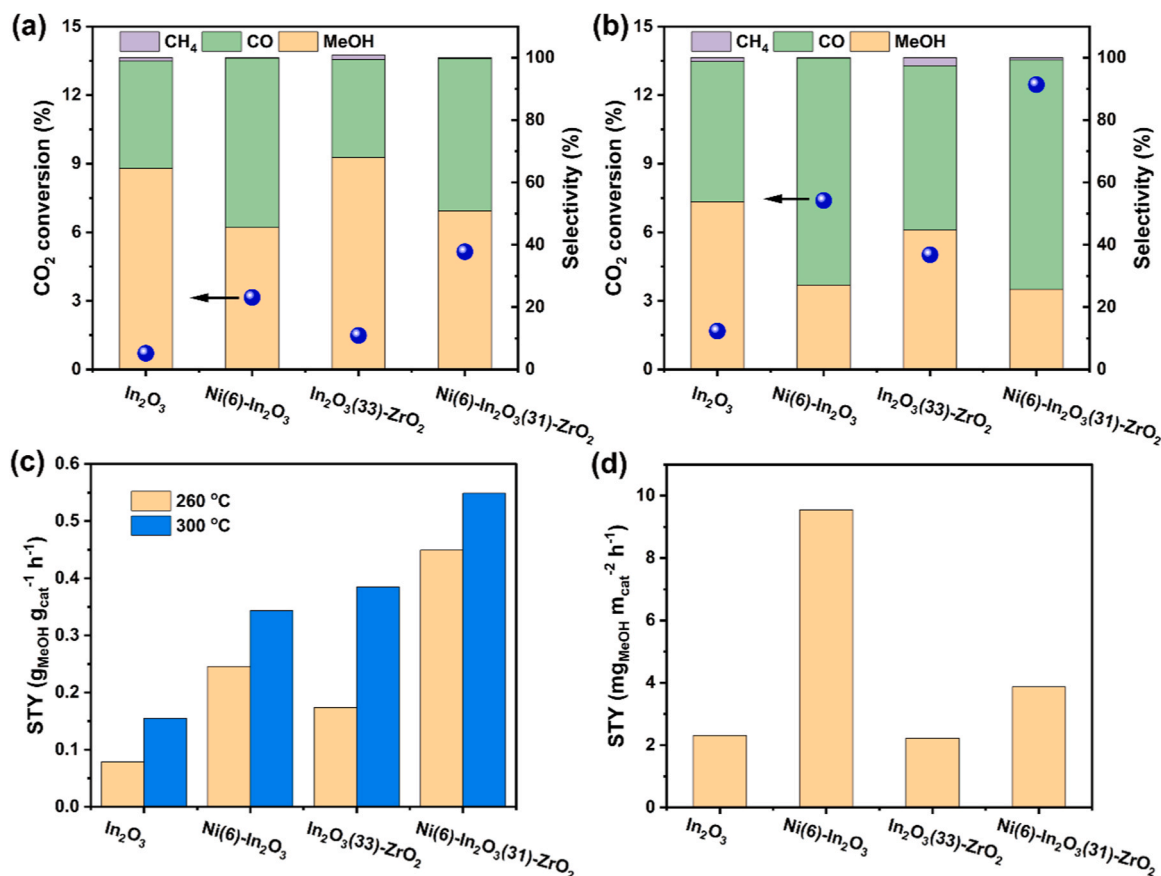

Fig. 1. Selectivity and CO$_2$ conversion during CO$_2$ hydrogenation over In$_2$O$_3$, Ni(6)-In$_2$O$_3$, In$_2$O$_3$(33)-ZrO$_2$ and Ni(6)-In$_2$O$_3$(31)-ZrO$_2$ catalysts at (a) 260 °C and (b) 300 °C. (c) Methanol space-time yield (STY) normalized by catalyst weight at 260 and 300 °C, and (d) Methanol space-time yield (STY) normalized by surface area over In$_2$O$_3$, Ni(6)-In$_2$O$_3$, In$_2$O$_3$(33)-ZrO$_2$ and Ni(6)-In$_2$O$_3$(31)-ZrO$_2$ catalysts at 300 °C. Reaction conditions: P = 30 bar, H$_2$/CO$_2$ = 3, and WHSV = 60,000 mL h^{-1} g$_{cat}^{-1}$.

promotion in the latter catalyst may be due to part of Ni ending up on ZrO_2. Fig. S2 compares the stability of $Ni(6)-In_2O_3$ and $Ni(6)-In_2O_3(31)$-ZrO_2 catalysts during CO_2 hydrogenation at 260 °C. Whereas both the activity and methanol rate of $Ni(6)-In_2O_3$ decreased during the reaction of 14 h, the activity and methanol rate of $Ni(6)-In_2O_3(31)$-ZrO_2 did not significantly change, indicating the stabilizing role of ZrO_2 with respect to catalyst performance.

3.3. Ni and ZrO₂ promotion

The XRD patterns of the used samples are shown in Fig. S3. The XRD patterns of the used $Ni(6)-In_2O_3$ and $Ni(6)-In_2O_3$-ZrO_2 samples are similar to those of the corresponding as-prepared samples with In_2O_3 as the main phase at low ZrO_2 content and an increasing shift of the diffraction lines due to the formation of t-ZrO_2 at higher ZrO_2 content in the used $In_2O_3(33)$-ZrO_2 and $Ni(6)-In_2O_3$-ZrO_2 samples. In contrast to the presence of t-ZrO_2 in as-prepared $Ni(6)$-ZrO_2, the main phase in the used catalyst is m-ZrO_2. The phase transformation is likely driven by the high water concentration during the reaction, as this catalyst exhibited a relatively high CO_2 conversion and high CH_4 selectivity. Such phase transformation was also reported for a Pd-In_2O_3-ZrO_2 catalyst [13]. The diffraction lines for used In_2O_3 and $Ni(6)-In_2O_3$ are sharper than those for corresponding as-prepared samples, indicating that the In_2O_3 particles agglomerated during CO_2 hydrogenation. The particle size and surface area of the used samples are shown in Table 1. The used $Ni(6)-In_2O_3$ sample contains larger particles of 19.1 nm than used In_2O_3 (12.5 nm), which can be attributed to a deeper reduction of In_2O_3 in $Ni(6)-In_2O_3$, caused by H_2 spillover from Ni. A similar phenomenon has been reported for Pd/In_2O_3 [21]. Particle agglomeration also occurs for the ZrO_2-containing samples, but the degree of sintering strongly decreases with increasing ZrO_2 content. Especially the samples with a ZrO_2 content of 44 wt% and higher show only a small increase in the In_2O_3/t-ZrO_2 particle size, indicating the promoting effect of ZrO_2 on the structure of the catalyst. This finding is further supported by Rietveld refinement, revealing an In_2O_3 particle size of ∼38 nm for $Ni(6)-In_2O_3$, which is substantially larger than the ∼6 nm observed for $Ni(6)-In_2O_3(31)$-ZrO_2 (Table S2). The variation in surface area is in keeping with the particle size trend (Table 1). These findings show that (i) In_2O_3 is prone to sintering, (ii) Ni enhances sintering, likely due to hydrogen spillover and deeper reduction of In_2O_3, and (iii) ZrO_2 stabilizes the dispersion of In_2O_3, even in the presence of Ni. Comparison to literature shows that sintering of In_2O_3 particles is a common

phenomenon, also observed for larger In_2O_3 particles. For instance, Pérez-Ramírez's group used FSP method to prepare In_2O_3 and $Ni-In_2O_3$ samples, with In_2O_3 particle sizes of 19 and 34 nm, respectively [22]. At nearly similar reaction conditions, these particles also sintered to respectively 29 and 43 nm [22].

The structure of the Ni species of $Ni(6)-In_2O_3$ and $Ni(6)-In_2O_3(31)$-ZrO_2 after the reaction was further characterized by XAS (Fig. 2). Ni K-edge XANES spectra of the Ni-containing samples are shown in Fig. 2a. The edge energy of 8344 eV in the as-prepared samples corresponds to that of the NiO reference, indicating that Ni is mainly in the +2 state. After reaction at 300 °C, the edge is located at lower energy, pointing to Ni reduction. As the edge energies are slightly higher than that of the Ni foil, it can be concluded that some Ni-oxide species remain in the used samples. The edge energy of used $Ni(6)-In_2O_3(31)$-ZrO_2 is higher than that of used $Ni(6)-In_2O_3$, suggesting a lower reduction degree in the Zr-containing samples. Linear combination fitting (LCF) of the XANES spectra confirms this, with metallic Ni contributions of 89 % for $Ni(6)$-In_2O_3 and 49 % for $Ni(6)-In_2O_3(31)$-ZrO_2 (Table S3). We speculate that sintering of In_2O_3 decreases the $Ni-In_2O_3$ interactions and benefits Ni reduction. The difference in Ni reduction degree can thus be linked to less pronounced sintering of $Ni(6)-In_2O_3(31)$-ZrO_2 compared to $Ni(6)$-In_2O_3. The presence of ZrO_2 in $Ni(6)-In_2O_3(31)$-ZrO_2 maintains a high In_2O_3 dispersion during the reaction compared to $Ni(6)-In_2O_3$. The higher reducibility of smaller In_2O_3 particles results in a stronger interaction with Ni, thereby impeding Ni reduction.

EXAFS at the Ni K-edge were recorded for as-prepared and used $Ni(6)-In_2O_3$ and $Ni(6)-In_2O_3(31)$-ZrO_2 samples. The k^3-weighted EXAFS and corresponding Fourier transforms of these spectra are shown in Figs. 2b, 2c and S4, while the fit results, including coordination distances (R) and coordination numbers (CN), are collected in Table S4. The fit results show that the first and second shells are dominated by Ni-O (R ∼2.0 Å) and Ni-O-In (R ∼3.3 Å) shells in the as-prepared $Ni(6)-In_2O_3$ and $Ni(6)-In_2O_3(31)$-ZrO_2 samples. A Ni-O-Ni (oxidic) shell with CN of ∼2 was observed in $Ni(6)-In_2O_3$, suggesting the presence of some Ni-oxide agglomerates. The Fourier transforms of the EXAFS spectra of the used samples are clearly different. The fit results show a decrease in the CN of the Ni-O and Ni-In (oxidic) shells together with the appearance of a metallic Ni-Ni shell. This points to the reduction of oxidic Ni species to metallic Ni during the reaction. The presence of a Ni-In (metallic) shell at ∼2.5 Å in used $Ni(6)-In_2O_3$ indicates some over-reduction of In, pointing to Ni-In alloy formation, as previously reported for $Ni-In_2O_3$ catalysts [3]. The formation of Ni-In alloy phases also dilutes the Ni

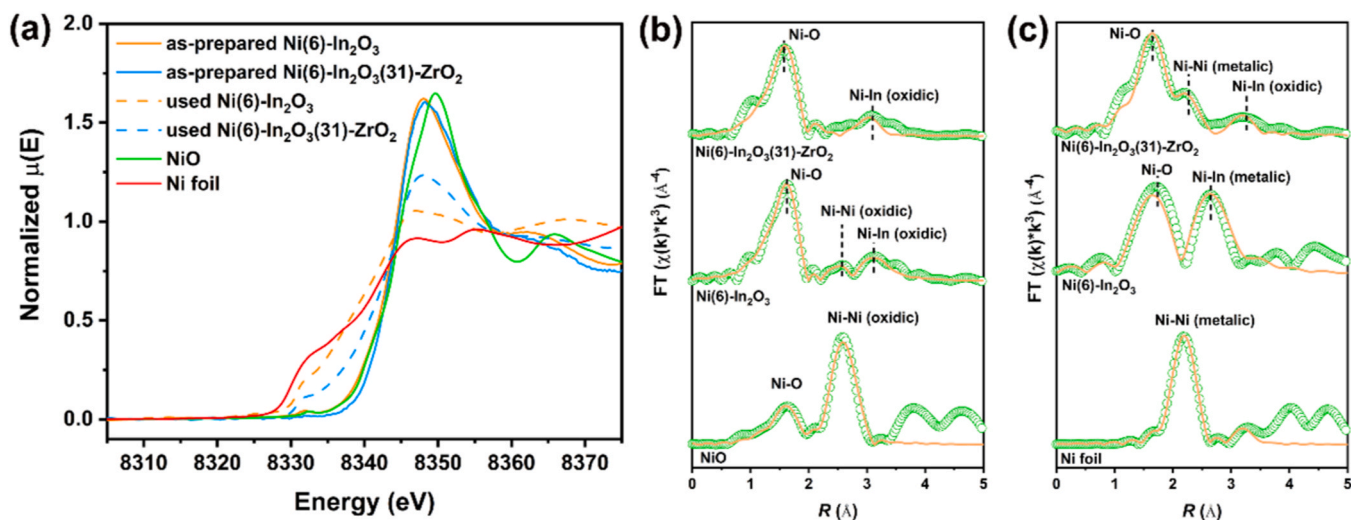**Fig. 2.** (a) Normalized XANES spectra at the Ni K-edge of the as-prepared and used $Ni(6)-In_2O_3$ and $Ni(6)-In_2O_3(31)$-ZrO_2 catalysts. EXAFS with model fit for the (b) as-prepared and (c) used $Ni(6)-In_2O_3$ and $Ni(6)-In_2O_3(31)$-ZrO_2 catalysts after activation in CO_2 hydrogenation for 12 h. Activation conditions: T = 300 °C, P = 30 bar, H_2/CO_2 = 3.

surface facets that otherwise would catalyze methanation. Differently, a Ni-Ni (metallic) shell with R ~2.2 Å was the only metallic shell observed in used Ni(6)-In$_2$O$_3$(31)-ZrO$_2$. This can suggest that the interactions between ZrO$_2$ and In$_2$O$_3$ hinder the reduction of In$_2$O$_3$. EXAFS analysis reveals a coordination number (CN) of ~2 for the metallic Ni-Ni shell in Ni-In$_2$O$_3$-ZrO$_2$ and a CN of ~3 for the metallic Ni-In shell in Ni-In$_2$O$_3$. These CNs are much smaller than the CNs numbers expected for nanoparticles (CN > 10). In fact, these CNs point to the presence of very small clusters of a few atoms. This is also evident from previous literature on Ni-In$_2$O$_3$ [3], who reported CNs of Ni-Ni shells of 1.4, 2.4, and 3.7 for 1, 5, and 15Ni-In$_2$O$_3$ (loading of Ni, wt%), indicative of well-dispersed Ni clusters in reduced Ni-In$_2$O$_3$ catalysts compared to bulk Ni metal and InNi$_3$ alloy with CNs of 12.

H$_2$-TPR was used to investigate the reduction behavior in the Ni-In$_2$O$_3$ and Ni-In$_2$O$_3$-ZrO$_2$ samples (Fig. 3). Ni(6)-In$_2$O$_3$ and Ni(6)-In$_2$O$_3$(31)-ZrO$_2$ display a similar reduction feature at 238 °C, corresponding to surface In$_2$O$_3$ reduction. This reduction temperature is lower than the surface reduction temperature of 258 °C of pure In$_2$O$_3$ [1]. The lower reduction temperature observed for the Ni-containing samples can be attributed to Ni doping in In$_2$O$_3$, which distorts the In$_2$O$_3$ lattice, thereby facilitating In$_2$O$_3$ reduction [8]. The smaller size of the In$_2$O$_3$ particles in the Ni-promoted samples compared to that of pure In$_2$O$_3$ may also contribute to the higher reducibility of In$_2$O$_3$ [23]. Quantification of this reduction peak reveals H$_2$ consumptions of 0.39 and 0.34 mmol/g$_{cat}$ for Ni(6)-In$_2$O$_3$ and Ni(6)-In$_2$O$_3$(31)-ZrO$_2$ samples, respectively (Table S5). This indicates that the addition of Zr slightly inhibits the reduction of surface In$_2$O$_3$. As reported in the literature [5,18], the formation of oxygen vacancies via the over-reduction of In$_2$O$_3$ results in disordered In$_2$O$_3$ and the formation of metallic In, ultimately leading to catalyst deactivation. ZrO$_2$ assists in stabilizing lattice oxygen atoms of In$_2$O$_3$ and suppressing the over-reduction to metallic In during the reaction. A peak at 286 °C in Ni(6)-In$_2$O$_3$ can be assigned to the reduction of NiO [8]. This peak shifts to a higher temperature in Ni(6)-In$_2$O$_3$(31)-ZrO$_2$ and Ni(6)-ZrO$_2$ samples, indicating the stabilizing effect of ZrO$_2$ on NiO reduction. The H$_2$/Ni ratio corresponding to this feature is 1.65 for Ni(6)-In$_2$O$_3$ and 1.44 for Ni(6)-In$_2$O$_3$(31)-ZrO$_2$, suggesting that part of H$_2$ is used to reduce In$_2$O$_3$ to In, caused by hydrogen spillover from metallic Ni. ZrO$_2$ is commonly regarded as a non-reducible oxide. The surface of ZrO$_2$ near metal particles experiences only minor reduction at elevated temperatures [24]. In this work, a ZrO$_2$ reference sample prepared by FSP (1.0 mL/min injection rate, surface area 204 m^2/g, mixture of t-ZrO$_2$ and m-ZrO$_2$ phases) exhibits a reduction peak at 484 °C. The difference in reduction behavior of ZrO$_2$

may be attributed to a difference in ZrO$_2$ crystallite size between this work (~5 nm) and the literature (~12 nm) [24]. In our previous works [23,25], we found that decreasing the size of In$_2$O$_3$ and CeO$_2$ particles below 10 nm results in enhanced reducibility. A similar phenomenon may occur with ZrO$_2$. The position of this peak shifts to a lower temperature and overlaps with the reduction peak in the NiO in the Ni(6)-ZrO$_2$ and Ni(6)-In$_2$O$_3$(31)-ZrO$_2$ samples. This also points to a role of hydrogen spillover from Ni, which is commonly observed for reduced metals on ZrO$_2$, as for instance for Pt/ZrO$_2$ [26].

We studied the differences in reaction kinetics between Ni(6)-In$_2$O$_3$(31)-ZrO$_2$ and Ni(6)-In$_2$O$_3$. The apparent activation energies for methanol synthesis and the reverse water-gas shift (rWGS) reaction are shown in Table S6 (Fig. S5). As can be expected the apparent activation energies for the rWGS reaction are higher than those for methanol synthesis. The apparent activation energies for methanol synthesis for Ni(6)-In$_2$O$_3$(31)-ZrO$_2$ is higher (65 kJ/mol) than for Ni(6)-In$_2$O$_3$ (44 kJ/mol). It is difficult to relate these differences in apparent activation energy to mechanistic aspects. A key structural difference between the two catalysts is the smaller size of In$_2$O$_3$ particles, which may affect the adsorption strength of CO$_2$-related reaction intermediates and the rate-controlling step. The apparent reaction orders of H$_2$ and CO$_2$ for methanol synthesis are shown in Table S6 (Fig. S6). The H$_2$ reaction orders for Ni(6)-In$_2$O$_3$(31)-ZrO$_2$ and Ni(6)-In$_2$O$_3$ are 2.2 and 1.5, while the CO$_2$ reaction orders are 0.3 and 0.4, respectively. The high H$_2$ reactions orders point to a rate-limiting step of strongly hydrogenated surface intermediate such as H$_2$CO* or H$_3$CO* with the CO$_2$ reaction orders, indicating a relatively high coverage with CO$_x$ intermediates. The apparent reaction orders of H$_2$ and CO$_2$ with respect to CO formation are given in Table S6 (Fig. S7). The CO$_2$ reaction orders for CO formation for the Ni(6)-In$_2$O$_3$ and Ni(6)-In$_2$O$_3$(31)-ZrO$_2$ catalysts are 0.4 and 0.3, respectively. While the H$_2$ reaction orders with respect to CO formation is ~0 for Ni(6)-In$_2$O$_3$(31)-ZrO$_2$, the CO rate of Ni(6)-In$_2$O$_3$ first increases with H$_2$ partial pressure (order ~1.3) and then decreases when the H$_2$ partial pressure exceeds 18 bar. Overall, the order in H$_2$ with respect to methanol is higher than with respect to CO, which is expected. The different H$_2$ reaction orders with respect to CO indicate that the active sites for CO formation in these two samples are different.

DRIFTS-SSITKA experiments were conducted to investigate relevant intermediates of methanol formation during CO$_2$ hydrogenation (Fig. 4). For the Ni(6)-In$_2$O$_3$(31)-ZrO$_2$ sample, we investigated the response to a switch of the reaction gas from ^{12}CO$_2$+H$_2$ to ^{13}CO$_2$+H$_2$ (CO$_2$:H$_2$:Ar = 1:3:1, gas flow rate = 50 mL/min, 1 bar) at 260 °C and 1 bar. The DRIFTS spectra obtained before and after the switch are given in Fig. 4a. These spectra contain bands at 2356 and 2017 cm^{-1}, corresponding to gaseous CO$_2$ and carbonyls (CO*), respectively. The bands at 1600 and 2850 cm^{-1} are assigned to the v(CH) and v_{as}(OCO) of formate in the C-H and C-O regions, respectively. These bands occur at lower wavenumbers after the isotopic switch from ^{12}CO$_2$+H$_2$ to ^{13}CO$_2$+H$_2$. We observe a substantial shift of the band at 1600 cm^{-1}, while the band at ~2850 cm^{-1} shows a small but significant shift to lower wavenumbers. The carbonates observed in the 1600–1200 cm^{-1} region (1507, 1450, 1362 cm^{-1}) do not exhibit such a shift, indicating that they are spectator species and are not exchanged at the time scale of the experiment. The evolution of surface intermediates determined by DRIFTS and reaction products obtained by MS during the switch is shown in Fig. 4b–e. This switch leads to a decrease in the intensity of the 2017 and 1600 cm^{-1} due to ^{12}C-labelled CO* and HCOO*, respectively, and an increase in the intensity of the 1959 and 1552 cm^{-1} bands due to ^{13}C-labelled CO* and HCOO*. Concomitantly, increasing amounts of ^{13}C-labelled methanol and CO are detected by MS. The surface residence time of H^{13}COO* (~380 s) is very close to the residence time of methanol (~377 s) detected by MS (^{13}CH$_3$OH, m/z = 33). The residence time of ^{13}CO* and gaseous CO detected by MS (^{13}CO, m/z = 29) are ~40 s and ~14 s, respectively. These residence times are much shorter than the residence time of HCOO*. These findings clearly show that methanol and CO are formed via distinctly different reaction pathways. The steady-state
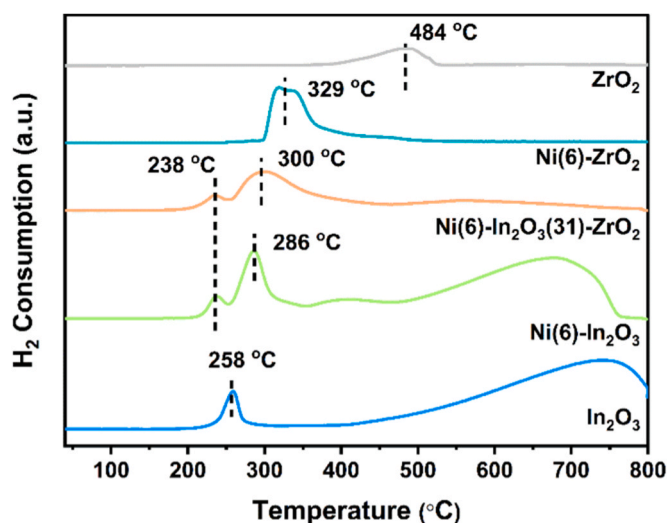

Fig. 3. H$_2$-TPR profiles of the as-prepared In$_2$O$_3$, Ni(6)-In$_2$O$_3$, Ni(6)-In$_2$O$_3$(31)-ZrO$_2$, Ni(6)-ZrO$_2$ and ZrO$_2$ samples.

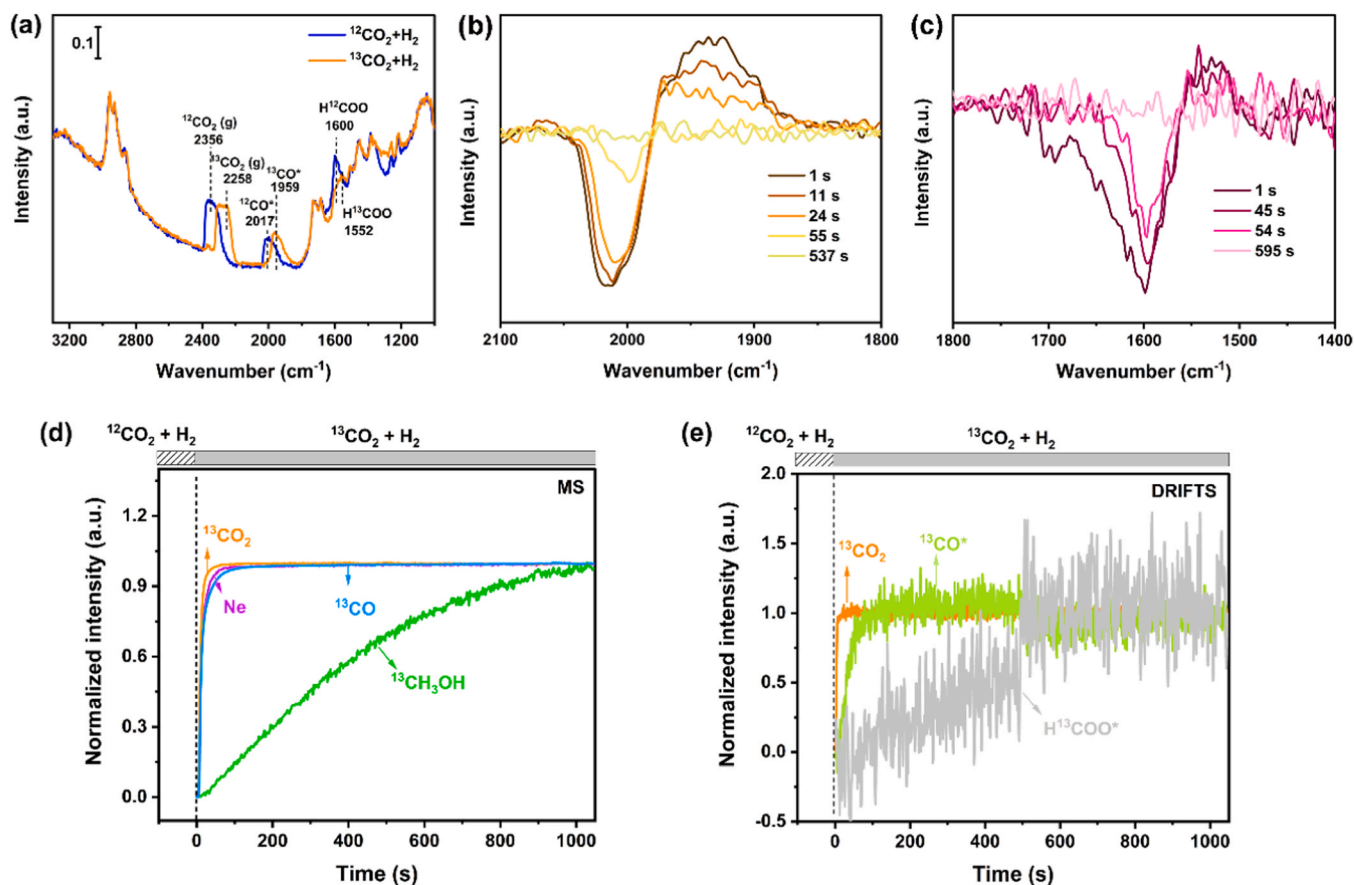**Fig. 4.** DRIFTS-SSITKA experiment involving a switch from $^{12}CO_2 + H_2$ to $^{13}CO_2 + H_2$ over Ni(6)-In$_2$O$_3$(31)-ZrO$_2$. (a) DRIFTS spectrum collected before and after the switch. Detailed time-resolved DRIFTS spectra during the switch in the (b) carbonyl region and (c) formate region. (d) Normalized MS signals of Ne ($m/z = 22$), $^{13}CO_2$ ($m/z = 45$), ^{13}CO ($m/z = 29$) and $^{13}CH_3OH$ ($m/z = 33$) recorded by MS. (e) Normalized IR signals of $^{13}CO_2$ (2258 cm^{-1}), $^{13}CO^*$ (1959 cm^{-1}) and H$^{13}COO^*$ (1552 cm^{-1}) by DRIFTS (reaction conditions: T = 260 °C, P = 1 bar, CO$_2$:H$_2$:Ar =1:3:1, gas flow rate = 50 mL/min, Ne inert tracer).

reaction kinetics indicate that one of the last hydrogenation steps is controlling the methanol formation rate. This could be the hydrogenation of CH$_3$O*. This leads to a tentative mechanism of consecutive adsorption of CO$_2$ and its hydrogenation to HCOO*, CH$_3$O* and finally methanol.

In situ IR spectroscopy was used to follow the evolution of surface intermediates for Ni(6)-In$_2$O$_3$ and Ni(6)-In$_2$O$_3$(31)-ZrO$_2$ during steady-state CO$_2$ hydrogenation and a subsequent switch to He (Fig. 5). These spectra were recorded in transmission mode at a total pressure of 10 bar. As the signal-to-noise ratio of the In$_2$O$_3$ samples was too low to record meaningful spectra, we used ZrO$_2$ prepared by FSP as a diluent. Reference measurements with ZrO$_2$ (Fig. S8) showed that exposure to a CO$_2$/H$_2$ mixture at 40 °C led to the formation of bicarbonate (HCO$_3^-$), monodentate carbonate (m-CO$_3^{2-}$) and bidentate carbonate (b-CO$_3^{2-}$) species. The bands of 1625 and 1225 cm^{-1} are due to HCO$_3^-$, those at 1422 and 1335 cm^{-1} are attributed to m-CO$_3^{2-}$, and those at 1633, 1528 and 1087 cm^{-1} can be assigned to b-CO$_3^{2-}$ [27,28]. Upon increasing the temperature to 260 °C, the intensity of the b-CO$_3^{2-}$ band increased, accompanied by the appearance of polydentate carbonates (p-CO$_3^{2-}$, broad band 1484 cm^{-1}) and weak features due to formate (HCOO*, 1564 and 1380 cm^{-1}) [29]. C-H vibrations of formate are absent, which is likely due to the very small amount of formates formed. Surface methoxy species were also not observed. Moreover, it was confirmed that FSP-derived ZrO$_2$ did not exhibit any CO$_2$ hydrogenation activity (260 °C, 30 bar, CO$_2$/H$_2$/N$_2$ = 10/30/10 mL/min). Despite the presence of carbonate on ZrO$_2$ in the IR spectra of the catalyst samples, these contributions are minor, and ZrO$_2$ does not show obvious signatures of formate and methoxy species. For the sample measurements, the IR

spectra were recorded in the reaction mixture (CO$_2$:H$_2$ = 1:3, 10 bar, 50 mL/min), while heating from 50 to 300 °C. After exposure of Ni(6)-In$_2$O$_3$ to this mixture at 50 °C, the spectra feature bands due to HCO$_3^-$ (1613 and 1225 cm^{-1}), m-CO$_3^{2-}$ (1422 and 1335 cm^{-1}) and b-CO$_3^{2-}$ (1633 and 1528 cm^{-1}) species [27,28]. Increasing the temperature to 300 °C, the intensities of the m-CO$_3^{2-}$ and H-CO$_3^-$ bands gradually decrease along with the appearance of bands corresponding to formate (HCOO*, 2970, 2872, 1590, 1570, 1384, 1365 cm^{-1}), methoxy (CH$_3$O*, 2920, 2822, 1141 and 1045 cm^{-1}) and polydentate carbonate (p-CO$_3^{2-}$, 1484 cm^{-1}) [27,30]. For Ni(6)-In$_2$O$_3$, we observe two additional bands at 1570 and 1590 cm^{-1}. According to the literature, the band at 1568 cm^{-1} corresponds to formate adsorbed on In$_2$O$_3$, while the band at 1561 cm^{-1} can be assigned to formate adsorption on ZrO$_2$ [29]. The formate species on Ni(6)-ZrO$_2$ gave rise to a band at 1593 cm^{-1} [31]. By analogy, we assign the band at 1570 cm^{-1} to formate on In$_2$O$_3$ and the one at 1590 cm^{-1} to formate on Ni sites. The minor difference in position might be caused by the likely smaller size of the Ni clusters in Ni-In$_2$O$_3$, while the inclusion of In into the Ni clusters can also be an explanation. Therefore, the surface contains formate species on Ni sites and on In$_2$O$_3$ in the Ni(6)-In$_2$O$_3$ catalyst. The corresponding spectra for Ni(6)-In$_2$O$_3$(31)-ZrO$_2$ evolve in the same way with temperature. The bands at 1568 and 1591 cm^{-1} observed at 300 °C can be attributed to formate. Compared to Ni(6)-In$_2$O$_3$, the 1568 cm^{-1} due to formate on In$_2$O$_3$ is stronger than the 1591 cm^{-1} due to formate on Ni sites. This can be explained by the higher In$_2$O$_3$ dispersion in the presence of ZrO$_2$ promoter. The spectra also indicate that Ni(6)-In$_2$O$_3$(31)-ZrO$_2$ contains more carbonates than Ni(6)-In$_2$O$_3$, mostly in the form of b-CO$_3^{2-}$ species.
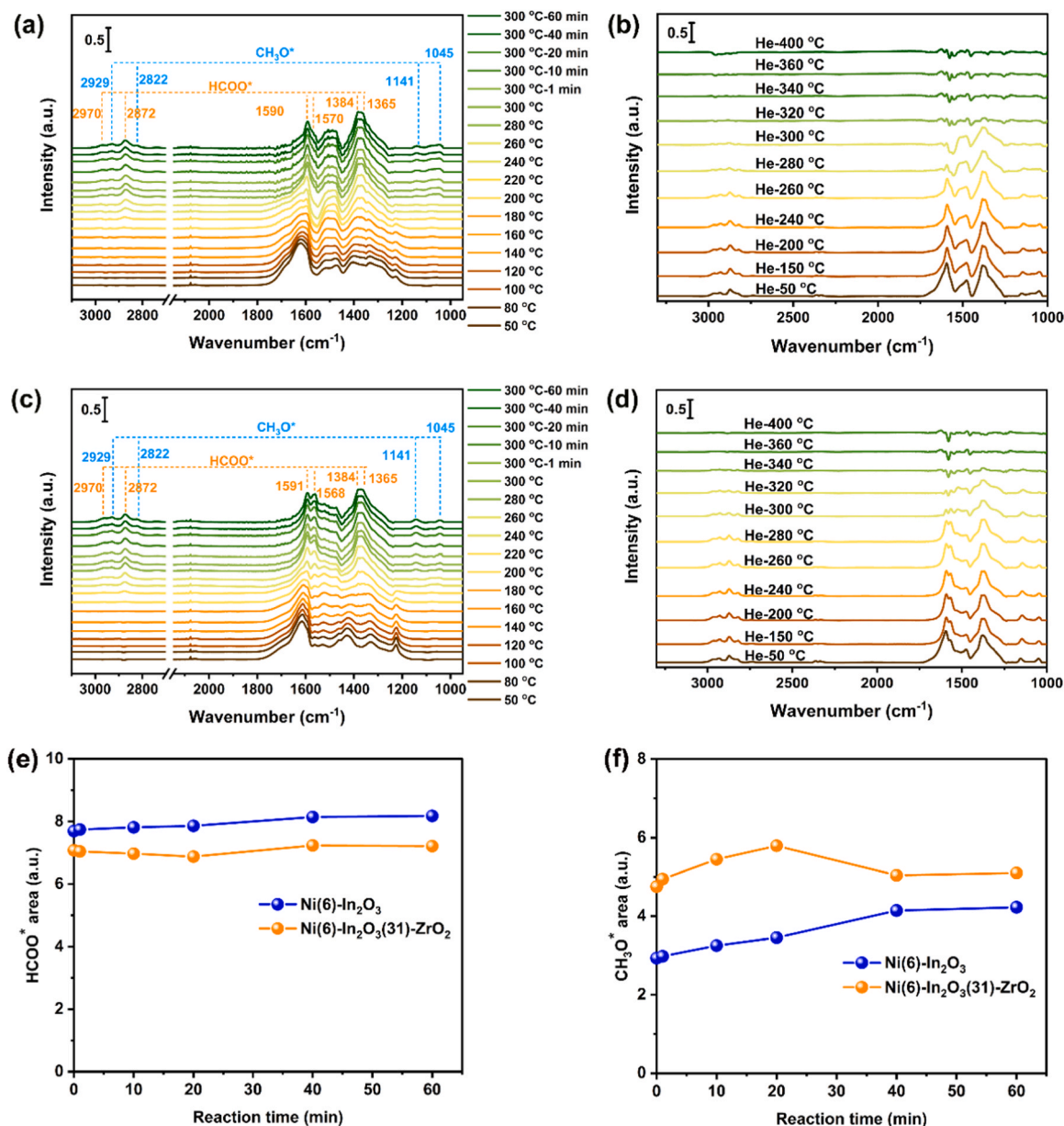
The amount of HCOO* and CH$_3$O* species was estimated by

Fig. 5. FTIR spectra during CO_2 hydrogenation over (a) Ni(6)-In_2O_3 and (c) Ni(6)-In_2O_3(31)-ZrO_2. FTIR spectra after switching the reaction gas to He (1 bar) at the temperature from 50 to 400 °C over (b) Ni(6)-In_2O_3 and (d) Ni(6)-In_2O_3(31)-ZrO_2. The evolution of peak area of (e) HCOO* and (f) CH_3O* collected from the spectra at 300 °C under reaction atmosphere for 60 min over Ni(6)/In_2O_3 and Ni(6)-In_2O_3(31)-ZrO_2 catalysts (peak areas normalized by catalyst weight; reaction conditions: CO_2:H_2 =1:3, gas flow rate = 50 mL/min, p = 10 bar).

integrating the areas of the corresponding IR bands at 2872 and 2929 cm^{-1}, respectively. The evolution of HCOO* and CH_3O* for Ni(6)-In_2O_3 and Ni(6)-In_2O_3(31)-ZrO_2 during CO_2 hydrogenation at 260 °C is shown in Fig. 5e and f. The intensity of the HCOO* band was stronger in Ni(6)-In_2O_3 than in Ni(6)-In_2O_3(31)-ZrO_2, which is likely due to the larger amount of In_2O_3 in the former sample. However, the formation of CH_3O* is faster on Ni(6)-In_2O_3(31)-ZrO_2 and, in the steady state, more CH_3O* is observed. This could be attributed to the stabilizing function in the conversion of formate to methoxy on ZrO_2.

To compare the adsorption strength of intermediates adsorbed on Ni(6)-In_2O_3 and Ni(6)-In_2O_3(31)-ZrO_2, we cooled the sample to 50 °C after the reaction in CO_2/H_2, followed by a switch to a He flow and a temperature increase to 400 °C (Fig. 5b and d). The formate bands at 1590 and 1570 cm^{-1} for Ni(6)-In_2O_3 disappeared at 280 °C, while these bands for Ni(6)-In_2O_3(31)-ZrO_2 only eroded at 300 °C. This suggests stronger adsorption of formate on the Zr-promoted sample. Also, carbonate

decomposition occurred at a higher temperature for Ni(6)-In_2O_3(31)-ZrO_2. These findings indicate that the structural promotion by ZrO_2, resulting in smaller In_2O_3 crystallites, leads to stronger adsorption of CO_2 and its hydrogenated reaction intermediates.

4. Conclusion

Ni(6)-In_2O_3(31)-ZrO_2 prepared by FSP presents a significantly higher methanol rate than In_2O_3, Ni(6)-In_2O_3 and In_2O_3(33)-ZrO_2 reference catalysts under CO_2 hydrogenation conditions, indicating that the promoting effect of Ni and ZrO_2 is additive and not synergistic. A comprehensive analysis of kinetic data, and *in situ* IR results reveals that Ni facilitates the hydrogenation of adsorbed CO_2 into formate and methoxy reaction into methanol, while ZrO_2 stabilizes small In_2O_3 particles and enhances its dispersion, promoting the conversion of formate to methoxy. The kinetic analysis indicates significant changes in the

reaction mechanism upon promotion, which are most likely due to the different particle sizes of In_2O_3.

CRediT authorship contribution statement

Nikolay Kosinov: Writing – review & editing, Supervision. **Hao Zhang:** Investigation. **Liang Liu:** Writing – original draft, Methodology, Investigation, Conceptualization. **Yu Gao:** Formal analysis. **Emiel J.M. Hensen:** Writing – review & editing, Supervision, Project administration, Funding acquisition, Conceptualization.

Declaration of Competing Interest

The authors declare that they have no known competing financial interests or personal relationships that could have appeared to influence the work reported in this paper.

Data availability

Data will be made available on request.

Acknowledgments

Appendix A. Supporting information

Supplementary data associated with this article can be found in the online version at doi:10.1016/j.apcatb.2024.124210.

References

[1] O. Martin, A.J. Martín, C. Mondelli, S. Mitchell, T.F. Segawa, R. Hauert, C. Drouilly, D. Curulla-Ferré, J. Pérez-Ramírez, Indium oxide as a superior catalyst for methanol synthesis by CO_2 hydrogenation, Angew. Chem. Int. Ed. 55 (2016) 6261–6265, https://doi.org/10.1002/anie.201600943.

[2] J. Wang, G. Li, Z. Li, C. Tang, Z. Feng, H. An, H. Liu, T. Liu, C. Li, A highly selective and stable ZnO-ZrO$_2$ solid solution catalyst for CO_2 hydrogenation to methanol, Sci. Adv. 3 (2017) e1701290, https://doi.org/10.1126/sciadv.1701290.

[3] M.S. Frei, C. Mondelli, R. García-Muelas, J. Morales-Vidal, M. Philipp, O. V. Safonova, N. López, J.A. Stewart, D.C. Ferré, J. Pérez-Ramírez, Nanostructure of nickel-promoted indium oxide catalysts drives selectivity in CO_2 hydrogenation, Nat. Commun. 12 (2021) 1960, https://doi.org/10.1038/s41467-021-22224-x.

[4] M.S. Frei, M. Capdevila-Cortada, R. García-Muelas, C. Mondelli, N. López, J. A. Stewart, D. Curulla Ferré, J. Pérez-Ramírez, Mechanism and microkinetics of methanol synthesis via CO_2 hydrogenation on indium oxide, J. Catal. 361 (2018) 313–321, https://doi.org/10.1016/j.jcat.2018.03.014.

[5] A. Tsoukalou, P.M. Abdala, D. Stoian, X. Huang, M.-G. Willinger, A. Fedorov, C. R. Müller, Structural evolution and dynamics of an In_2O_3 catalyst for CO_2 hydrogenation to methanol: an operando XAS-XRD and in situ TEM study, J. Am. Chem. Soc. 141 (2019) 13497–13505, https://doi.org/10.1021/jacs.9b04873.

[6] X. Jiang, X. Nie, Y. Gong, C.M. Moran, J. Wang, J. Zhu, H. Chang, X. Guo, K. S. Walton, C. Song, A combined experimental and DFT study of H_2O effect on In_2O_3/ZrO2 catalyst for CO_2 hydrogenation to methanol, J. Catal. 383 (2020) 283–296, https://doi.org/10.1016/j.jcat.2020.01.014.

[7] M.S. Frei, C. Mondelli, R. Garcia-Muelas, K.S. Kley, B. Puertolas, N. Lopez, O. V. Safonova, J.A. Stewart, D. Curulla Ferre, J. Perez-Ramirez, Atomic-scale engineering of indium oxide promotion by palladium for methanol production via CO_2 hydrogenation, Nat. Commun. 10 (2019) 3377, https://doi.org/10.1038/s41467-019-11349-9.

[8] J. Zhu, F. Cannizzaro, L. Liu, H. Zhang, N. Kosinov, I.A.W. Filot, J. Rabeah, A. Brückner, E.J.M. Hensen, Ni–In synergy in CO_2 hydrogenation to methanol, ACS Catal. 11 (2021) 11371–11384, https://doi.org/10.1021/acscatal.1c03170.

[9] Z. Han, C. Tang, J. Wang, L. Li, C. Li, Atomically dispersed Pt^{n+} species as highly active sites in Pt/In$_2$O$_3$ catalysts for methanol synthesis from CO_2 hydrogenation, J. Catal. 394 (2021) 236–244, https://doi.org/10.1016/j.jcat.2020.06.018.

[10] M.S. Frei, C. Mondelli, A. Cesarini, F. Krumeich, R. Hauert, J.A. Stewart, D. Curulla Ferré, J. Pérez-Ramírez, Role of zirconia in indium oxide-catalyzed CO_2 hydrogenation to methanol, ACS Catal. 10 (2020) 1133–1145, https://doi.org/10.1021/acscatal.9b03305.

[11] C. Yang, C. Pei, R. Luo, S. Liu, Y. Wang, Z. Wang, Z.-J. Zhao, J. Gong, Strong electronic oxide–support interaction over In_2O_3/ZrO$_2$ for highly selective CO_2 hydrogenation to methanol, J. Am. Chem. Soc. 142 (2020) 19523–19531, https://doi.org/10.1021/jacs.0c07195.

[12] X. Zhang, A.V. Kirilin, S. Rozeveld, J.H. Kang, G. Pollefeyt, D.F. Yancey, A. Chojecki, B. Vanchura, M. Blum, Support effect and surface reconstruction in In_2O_3/m-ZrO$_2$ catalyzed CO_2 hydrogenation, ACS Catal. 12 (2022) 3868–3880, https://doi.org/10.1021/acscatal.2c00207.

[13] T. Pinheiro Araújo, C. Mondelli, M. Agrachev, T. Zou, P.O. Willi, K.M. Engel, R. N. Grass, W.J. Stark, O.V. Safonova, G. Jeschke, S. Mitchell, J. Pérez-Ramírez, Flame-made ternary Pd-In$_2$O$_3$-ZrO$_2$ catalyst with enhanced oxygen vacancy generation for CO_2 hydrogenation to methanol, Nat. Commun. 13 (2022) 5610, https://doi.org/10.1038/s41467-022-33391-w.

[14] T.P. Araújo, J. Morales-Vidal, G. Giannakakis, C. Mondelli, H. Eliasson, R. Erni, J. A. Stewart, S. Mitchell, N. López, J. Pérez-Ramírez, Reaction-induced metal-metal oxide interactions in Pd-In$_2$O$_3$/ZrO$_2$ catalysts drive selective and stable CO2 hydrogenation to methanol, Angew. Chem. Int. Ed. 62 (2023) e202306563, https://doi.org/10.1002/anie.202306563.

[15] Z. Zhang, C. Shen, K. Sun, C.-J. Liu, Improvement in the activity of Ni/In$_2$O$_3$ with the addition of ZrO$_2$ for CO_2 hydrogenation to methanol, Catal. Commun. 162 (2022) 106386, https://doi.org/10.1016/j.catcom.2021.106386.

[16] Z. Lu, J. Wang, K. Sun, S. Xiong, Z. Zhang, C.-j Liu, CO_2 hydrogenation to methanol over Rh/In$_2$O$_3$–ZrO$_2$ catalyst with improved activity, Green Chem. Eng. 3 (2022) 165–170, https://doi.org/10.1016/j.gce.2021.12.002.

[17] Z. Lu, K. Sun, J. Wang, Z. Zhang, C. Liu, A highly active au/In$_2$O$_3$-ZrO$_2$ catalyst for selective hydrogenation of CO_2 to methanol, Catalysts 10 (2020) 1360, https://doi.org/10.3390/catal10111360.

[18] K. Sun, C. Shen, R. Zou, C.-j Liu, Highly active Pt/In$_2$O$_3$-ZrO$_2$ catalyst for CO_2 hydrogenation to methanol with enhanced CO tolerance: the effects of ZrO$_2$, Appl. Catal., B 320 (2023) 122018, https://doi.org/10.1016/j.apcatb.2022.122018.

[19] X. Jia, X. Zhang, N. Rui, X. Hu, C.-j Liu, Structural effect of Ni/ZrO$_2$ catalyst on CO_2 methanation with enhanced activity, Appl. Catal. B 244 (2019) 159–169, https://doi.org/10.1016/j.apcatb.2018.11.024.

[20] J.F.M. Simons, T.J. de Heer, R.C.J. van de Poll, V. Muravev, N. Kosinov, E.J. M. Hensen, Structure sensitivity of CO_2 hydrogenation on Ni revisited, J. Am. Chem. Soc. 145 (2023) 20289–20301, https://doi.org/10.1021/jacs.3c04284.

[21] M.S. Frei, C. Mondelli, R. García-Muelas, K.S. Kley, B. Puértolas, N. López, O. V. Safonova, J.A. Stewart, D. Curulla Ferré, J. Pérez-Ramírez, Atomic-scale engineering of indium oxide promotion by palladium for methanol production via CO_2 hydrogenation, Nat. Commun. 10 (2019) 3377, https://doi.org/10.1038/s41467-019-11349-9.

[22] T. Pinheiro Araújo, J. Morales-Vidal, T. Zou, R. García-Muelas, P.O. Willi, K. M. Engel, O.V. Safonova, D. Faust Akl, F. Krumeich, R.N. Grass, C. Mondelli, N. López, J. Pérez-Ramírez, Flame spray pyrolysis as a synthesis platform to assess metal promotion in In_2O_3-catalyzed CO_2 hydrogenation, Adv. Energy Mater. 12 (2022) 2103707, https://doi.org/10.1002/aenm.202103707.

[23] L. Liu, B. Mezari, N. Kosinov, E.J.M. Hensen, Al promotion of In_2O_3 for CO_2 hydrogenation to methanol, ACS Catal. (2023) 15730–15745, https://doi.org/10.1021/acscatal.3c04620.

[24] J. Ren, X. Qin, J.-Z. Yang, Z.-F. Qin, H.-L. Guo, J.-Y. Lin, Z. Li, Methanation of carbon dioxide over Ni–M/ZrO$_2$ (M=Fe, Co, Cu) catalysts: Effect of addition of a second metal, Fuel Process. Technol. 137 (2015) 204–211, https://doi.org/10.1016/j.fuproc.2015.04.022.

[25] V. Muravev, A. Parastaev, Y. van den Bosch, B. Ligt, N. Claes, S. Bals, N. Kosinov, E. J.M. Hensen, Size of cerium dioxide support nanocrystals dictates reactivity of highly dispersed palladium catalysts, Science 380 (2023) 1174–1179, https://doi.org/10.1126/science.adf9082.

[26] Z. Tang, P. Liu, H. Cao, S. Bals, H.J. Heeres, P.P. Pescarmona, Pt/ZrO2 prepared by atomic trapping: an efficient catalyst for the conversion of glycerol to lactic acid with concomitant transfer hydrogenation of cyclohexene, ACS Catal. 9 (2019) 9953–9963, https://doi.org/10.1021/acscatal.9b02139.

[27] A.R. Richard, M. Fan, Low-pressure hydrogenation of CO2 to CH3OH using Ni-In-Al/SiO2 catalyst synthesized via a phyllosilicate precursor, ACS Catal. 7 (2017) 5679–5692, https://doi.org/10.1021/acscatal.7b00848.

[28] Z. Feng, C. Tang, P. Zhang, K. Li, G. Li, J. Wang, Z. Feng, C. Li, Asymmetric sites on the ZnZrO$_x$ catalyst for promoting formate formation and transformation in CO_2 HYdrogenation, J. Am. Chem. Soc. 145 (2023) 12663–12672, https://doi.org/10.1021/jacs.3c02248.

[29] T.-y Chen, C. Cao, T.-b Chen, X. Ding, H. Huang, L. Shen, X. Cao, M. Zhu, J. Xu, J. Gao, Y.-F. Han, Unraveling highly tunable selectivity in CO_2 hydrogenation over bimetallic In-Zr oxide catalysts, ACS Catal. 9 (2019) 8785–8797, https://doi.org/10.1021/acscatal.9b01869.

[30] H. Zhao, R. Yu, S. Ma, K. Xu, Y. Chen, K. Jiang, Y. Fang, C. Zhu, X. Liu, Y. Tang, L. Wu, Y. Wu, Q. Jiang, P. He, Z. Liu, L. Tan, The role of Cu$_1$–O$_3$ species in single-atom Cu/ZrO$_2$ catalyst for CO_2 hydrogenation, Nat. Catal. 5 (2022) 818–831, https://doi.org/10.1038/s41929-022-00840-0.

[31] R. Ye, L. Ma, X. Hong, T.R. Reina, W. Luo, L. Kang, G. Feng, R. Zhang, M. Fan, R. Zhang, J. Liu, Boosting low-temperature CO_2 hydrogenation over Ni-based

catalysts by tuning strong metal-support interactions, Angew. Chem. Int. Ed. 63 (2024) e202317669, https://doi.org/10.1002/anie.202317669.